



HAL
open science

A self-supervised learning framework based on physics-informed and convolutional neural networks to identify local anisotropic permeability tensor from textiles 2D images for filling pattern prediction

John Hanna, José Aguado, Sebastien Comas-Cardona, Yves Le Guennec,
Domenico Borzacchiello

► To cite this version:

John Hanna, José Aguado, Sebastien Comas-Cardona, Yves Le Guennec, Domenico Borzacchiello. A self-supervised learning framework based on physics-informed and convolutional neural networks to identify local anisotropic permeability tensor from textiles 2D images for filling pattern prediction. *Composites Part A: Applied Science and Manufacturing*, 2024, 179, pp.108019. 10.1016/j.compositesa.2024.108019 . hal-04586152

HAL Id: hal-04586152

<https://hal.science/hal-04586152>

Submitted on 27 May 2024

HAL is a multi-disciplinary open access archive for the deposit and dissemination of scientific research documents, whether they are published or not. The documents may come from teaching and research institutions in France or abroad, or from public or private research centers.

L'archive ouverte pluridisciplinaire **HAL**, est destinée au dépôt et à la diffusion de documents scientifiques de niveau recherche, publiés ou non, émanant des établissements d'enseignement et de recherche français ou étrangers, des laboratoires publics ou privés.

A self-supervised learning framework based on physics-informed and convolutional neural networks to identify local anisotropic permeability tensor from textiles 2D images for filling pattern prediction

John M. Hanna^{a,b}, José V. Aguado^a, Sebastien Comas-Cardona^a, Yves Le Guennec^b, Domenico Borzacchiello^a

^aNantes Université, Ecole Centrale Nantes, CNRS, GeM, UMR 6183, 1 Rue de la Noë, 44300 Nantes, France

^bNantes Université, IRT Jules Verne, 44340 Bouguenais, France

Abstract

In liquid composite molding processes, variabilities in material and process conditions can lead to distorted flow patterns during filling. These distortions appear not only within the same part but also from one part to another. Notably, minor deviations in the dry fibrous textiles cause local permeability changes, resulting in flow distortions and potential defects. Traditional permeability models fall short in predicting these localized fluctuations, especially for anisotropic textiles, whereas reliance on homogeneous permeability models creates substantial discrepancies between forecasted and observed filling patterns. This study presents a self-supervised framework that determines in-plane permeability tensor field of textiles from an image of that textile in dry state. Data from central injection experiments is used for training, including flow images and pressure inlet data. This work demonstrates that this model proficiently predicts flow patterns in unobserved experiments and captures local flow distortions, even when trained on a relatively small dataset of experiments.

Keywords: flow in porous media, permeability field, macroscopic porous media, physics-informed neural networks, convolutional neural networks.

1. Introduction

1.1. Motivation and outline

Liquid Composite Molding (LCM) is a set of manufacturing techniques wherein a dry fibrous reinforcement undergoes impregnation by a liquid resin within a sealed cavity [1]. The flow of resin within the fibrous medium is described by Darcy's law, given by:

$$\mathbf{v} = -\frac{1}{\mu}\mathbf{K} \cdot \nabla p \quad (1)$$

where \mathbf{v} represents the volume average flow velocity, μ is the viscosity of the liquid, ∇p denotes the pressure gradient, and \mathbf{K} is the second-order permeability tensor of the textile which is related to the pore-scale microstructure geometry of the structure. Properly estimating this permeability tensor is pivotal for accurate predictions of the filling pattern, defining the evolution of the flow front within the fibrous reinforcement. Such precise predictions are instrumental in preempting the onset of structural flaws in the final product, such as incomplete filling and dry spots.

Variabilities within and between textile samples can arise due to fabric intrinsic geometrical defects, mishandling, misalignment, operator errors, and other factors. These inconsistencies can result in marked deviations between the actual and anticipated filling patterns, subsequently leading to variations in the quality of the manufactured parts. Two reviews list potential variabilities and defects occurring during structural composite manufacturing [2, 3].

Moreover, the existing experimental measurement techniques show inconsistencies among each other. Several international benchmarks have shown significant discrepancies between experimental measurements from different test benches

[4, 5, 6]. The reasons of variations can come from the geometrical control of the cavity, the sensors, the fluid used, the operator and the 1D, 2D, transient or steady nature of the injection. Following these investigations and recommendations, an experimental ISO standard has been very recently released [7] in order to measure an average permeability of anisotropic fibrous textiles. In addition, an international benchmark, entirely dedicated to numerical predictions from 3D tomographic images, was published and shows variations in results depending on the numerical approaches used to simulate the flow and to extract the average value of the permeability [8].

Most existing techniques for determining permeability provide average approximations over the studied domain, disregarding local effects. Alternatively, some methods focus on identifying permeability at the fiber scale, which is impractical to use for macro-scale porous media due to computational limitations. Therefore, there is a need for approaches that can capture the local variations in permeability within the porous media while still being applicable at a macroscopic scale. Previous studies identified local isotropic permeability fields for random mats [9, 10].

The methods to characterize the permeability can be roughly divided into four major groups: 1. Analytical models, 2. Experimental techniques, 3. Numerical homogenization and up-scaling techniques and 4. Machine learning techniques.

Empirical analytical models exist to estimate the permeability based on the geometry of the reinforcement. One of the most famous models is the Kozeny-Carmen model [11, 12]. The permeability tensor is estimated as follows:

$$\mathbf{K} = \frac{R^2}{4k} \frac{(1 - V_f)^3}{V_f^2} \mathbf{I}, \quad (2)$$

where V_f is the fibre-volume fraction, R is the fiber radius, k is called Kozeny constant and \mathbf{I} is the identity tensor. The predicted permeability is isotropic, which is an oversimplification for most fibrous structures. A modification was proposed by [13] where different k constants are chosen for different directions adding the anisotropy into the model.

The previously mentioned models only have the fiber radius as a geometry parameter, while the rest of the geometrical features are taken into account through empirical constants in the model that need to be identified using a fitting procedure on experimental data. This issue was dealt with by [14] where they developed a more inclusive model for unidirectional reinforcement. The issue still prevails for other types of fibrous media whose relevant features are not easily identified. The empirical laws suffer from not being tailored to the specificity of each reinforcement and do not offer an estimation of the permeability as a field, indeed, most of the local defects in a textile cannot be described using the same geometrical features as in the standard models.

Experimental methods are commonly employed to identify the permeability for each specific reinforcement [15]. These methods typically involve controlling either the pressure or velocity and measuring the other. Average values are then calculated, and the permeability is evaluated using Darcy's law. In the context of resin transfer molding, two main categories of experiments are typically conducted: unidirectional flow experiments [16, 17] and radial (central injection) experiments [18, 19]. A 3D central injection framework along with an optimization technique to measure the 3D permeability tensor was developed [20]. However, these experimental techniques have limitations, including being time-consuming and challenging to perform. Furthermore, the resulting permeability values obtained from these experiments represent average values over the entire domain, disregarding local effects within the fibrous media as in the case of empirical laws.

Numerical homogenization methods offer an interesting alternative to experimental techniques, as they are typically less complicated and time-consuming, compared to the latter. These methods aim to virtually replicate the experimental setup in a representative volume element (RVE) by fixing either the pressure or velocity and performing a high-fidelity simulation at the microscopic scale to estimate a proper average of the other parameter over the RVE. Numerical solvers,

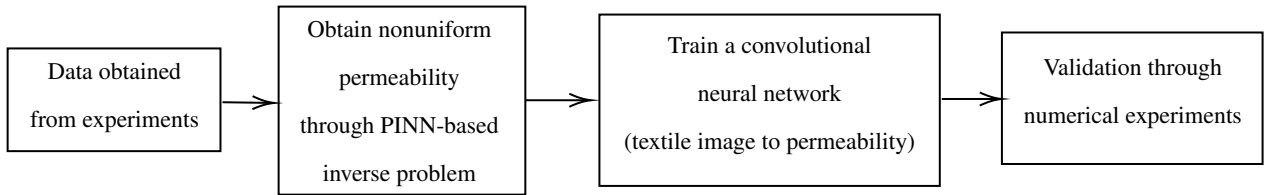
based on Computational Fluid Dynamics [14, 21, 22] or the Lattice Boltzmann Method [23, 24], are commonly employed. However, these techniques are more applicable to identifying the permeability of microstructures and become computationally complex when dealing with macroscale fibrous media. Additionally, obtaining knowledge of the porous media domain is crucial, which can be acquired through imaging techniques like tomography. Alternatively, a virtual reconstruction of the porous media can be employed to establish the relationship between the porous media properties and permeability.

Machine learning can certainly be used to address the discussed challenges due to its powerful prediction capabilities. Recently, machine learning techniques have been successfully applied to solve diverse problems in sciences and engineering [25, 26]. One of the fast-growing techniques is Physics-Informed Neural Networks (PINN) which was developed by [27]. PINN merges the physics and data knowledge in a combined loss function which offers a solution to problems with low-data regimes. It has been applied to problems involving solid mechanics [28], fluid mechanics [29], magnetic problems [30], and flow in porous media [31, 32]. The related literature is presented in more detail in the forthcoming section 1.3.

1.2. Scope of the current work

The present study tackles the challenge of estimating the permeability tensor field of a dry 2D plain-weave textile using neural networks based on its image representation. Notably, the prevailing body of literature primarily emphasizes the employment of convolutional neural networks (CNN) trained on extensive datasets of labeled images, either authentic or synthetic. These labels, representing the permeability values, are generally derived either through experimental measurements or by leveraging high-fidelity CFD solvers coupled with adequate homogenization techniques. Conversely, the methodology developed in this paper deals with a more constrained dataset, encompassing only 34 unlabelled experimental images. Since the used approach does not necessitate permeability labeling, it avoids the need for prior assumptions regarding the flow model at the microscopic scale. The model introduced in this paper is trained with an objective to minimize the distance between predicted and actual filling patterns, relying solely on flow imagery and pressure data from a single sensor located at the flow inlet. This intrinsic label estimation during training categorizes the methodology as self-supervised. The framework proposed in this manuscript relies on two separate fitting stages. Initially, permeabilities are estimated by addressing an inverse problem through PINNs, utilizing flow front imagery stemming from radial flow experiments coupled with inlet pressure measurements. Afterwards, a second regressor model (CNN) is trained on smaller crops of the original images correlating the permeability tensor with the local textile configuration. After the training phase is done, prediction of the permeability field can be done using only an image of the fabric in the dry state. The full training procedure along with the explanation of the model deployment is shown in figure 1.

Training stages



Deployment

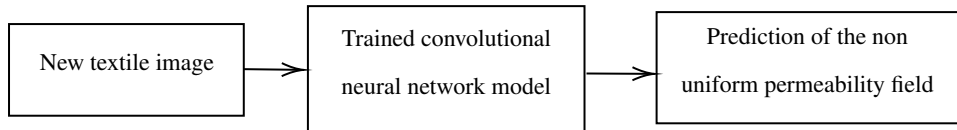


Figure 1: Diagram explaining the training stages of the model along with the deployment methodology.

1.3. Related work

1.3.1. Inverse problems with PINN

PINN have garnered significant attention for their efficacy in addressing inverse problems pertaining to systems governed by PDEs. Uncertain or latent parameters can be identified, including material properties that are not directly measurable. Central to this approach is the treatment of these unknown properties as trainable parameters within the neural model. Through simultaneous minimization of both the residual of the governing PDEs and the data discrepancy, PINNs not only learn the solution of the PDE system but also identify the missing parameters of the governing equations. PINN was introduced to solve a generic PDE with an unknown homogeneous material parameter with the knowledge of the solution on scattered points in the domain [27]. Using this methodology, several inverse problems have been solved. The technique was applied to solve for the density in high-speed flows [33]. It was also applied to obtain the hydraulic conductivity in unsteady 1D groundwater flows [34]. In another work, the authors obtained the permeability field in steady 2D natural-state geothermal system using pressure and temperature generated data [35]. This was done by having a neural network to approximate the permeability as a function of space. Other problems were solved in nano-optics [36], heat transfer [37], transport in porous media [38], and supersonic flows [39].

1.3.2. Image-based permeability identification

Some novel research work has a similar framework to the one adopted in this paper. However, it must be noted that all the former work deals with microscopic scale porous media images. Whereas, in this paper, the methodology is developed for macroscale fibrous porous media images. It was shown that feedforward neural networks and CNN are capable of directly calculating permeability where the inputs to the feedforward neural network are geometric properties of the porous media and the input to the CNN is porous media images [40]. In another work, a framework is developed to predict the porosity, permeability, and tortuosity of microstructure porous media from images using a CNN [41]. The authors built 100,000 virtual porous media generated by the random deposition method [42, 43]. LBM simulations are then performed on all the images to provide an estimation of the porosity, permeability, and tortuosity. A CNN is finally used for the supervised learning task. In this sense, the CNN learns to map images to the simulation results in a way that is computationally inexpensive and much faster than the original model used to generate the dataset.

A similar framework is presented but is applied to predict the diffusivity of porous media [44]. The authors generated a big dataset of virtual porous media images, and then performed LBM simulations to calculate the diffusivity. Finally, they trained a CNN using the generated dataset.

In another work, the authors developed a physics-informed CNN to predict the permeability from microstructure porous media images [45]. The framework is similar to that of [41] where porous media images are generated using the Voronoi tessellation algorithm. This is followed by LBM simulations of the porous media images. Finally, a physics-informed CNN is used for the supervised learning task. This is done by including porosity and specific surface area as inputs to the neural network along with the images. It was shown that this modification to the CNN provided better results than applying a regular CNN.

The same methodology of using a high-fidelity simulation applied to many porous media images to build an image-permeability dataset, then training a CNN was adopted in many applications involving porous media. The methodology was applied for gas diffusion layer materials [46], rock mechanics [47, 48, 49], and to fibrous porous media [50].

2. Experimental setup and available Data

2.1. Foreword

The present data were produced through 2D central injection experiments that were performed by Comas-Cardona at CACM (Centre for Advanced Composite Materials) at the University of Auckland (NZ) [51, 52].

2.2. Materials of the study

2.2.1. Liquid

The liquid used in this study is a mineral oil whose viscosity is $0.15 \text{ Pa}\cdot\text{s}$ at 20°C and has been measured on a Brookfield viscometer.

2.2.2. Textile

The textile of interest is a glass fiber plain weave (PW) whose areal weight has been measured and is $822 \text{ g}/\text{m}^2$. It should be noted that the same fabric was used to produce the samples of all the experiments.

At first, an image of the dry fabric (2D plain weave) is taken using a lightbox setup [51]. An example of the image is shown in figure 2. In the lightbox setup, white light is transmitted through the textile. Light intensity is proportional to the areal weight of the textile. Two images are taken, the first one corresponds to the transmitted light without the textile and the second one corresponds to the transmitted light with the textile sample. Then, a difference is made pixel-wise between both images. Therefore, in white one can see the fiber tows at 0° and 90° of the weave, and in black the holes (opened areas) between the tows. The liquid resin will flow in the darker areas (opened areas). The calibration of the images has been done and is $0.2338 \text{ mm}/\text{px}$.

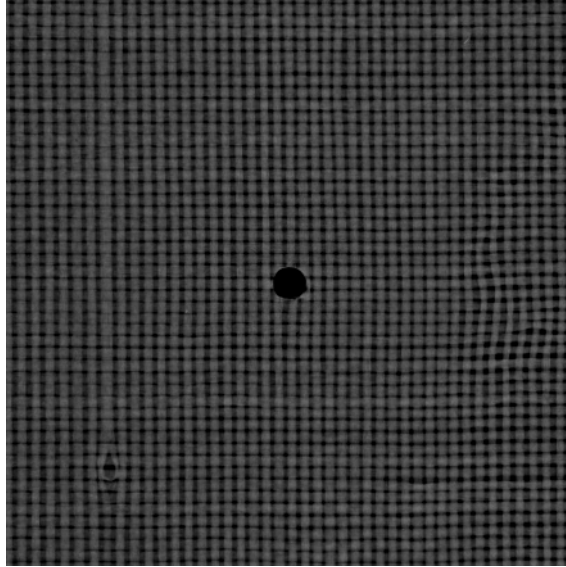


Figure 2: Lighbox image of the 2D plain weave textile used in the experiment. The image size is 1155×1155 pixels corresponding to 27×27 cm^2 .

The porosity of the tested textile is calculated for each sample using the mass of the ply m , the area of the ply A , the thickness of the ply h (measured as the cavity height between the compression platens), and glass density $\rho_f = 2.6 \text{ g/cm}^3$. According to the calculations, the samples have an average porosity of 0.45.

2.3. Injection Bench

The apparatus for the experiments is shown in figure 3 [52]. The apparatus consists of a fixed bottom transparent glass plate, a top moving stainless steel platen, a textile fabric, a tilted mirror, a camera, a pressure bucket, and an injection gate equipped with a pressure transducer. The top and bottom platens are mounted into a universal testing machine. After closing the top platen on the textile fabric at a given thickness, the resin inlet valve at the pressure bucket is opened. The resin will flow from the central injection point into the textile as the time goes on. For more details on the injection bench, the reader can refer to the work by Swery et al. [52].

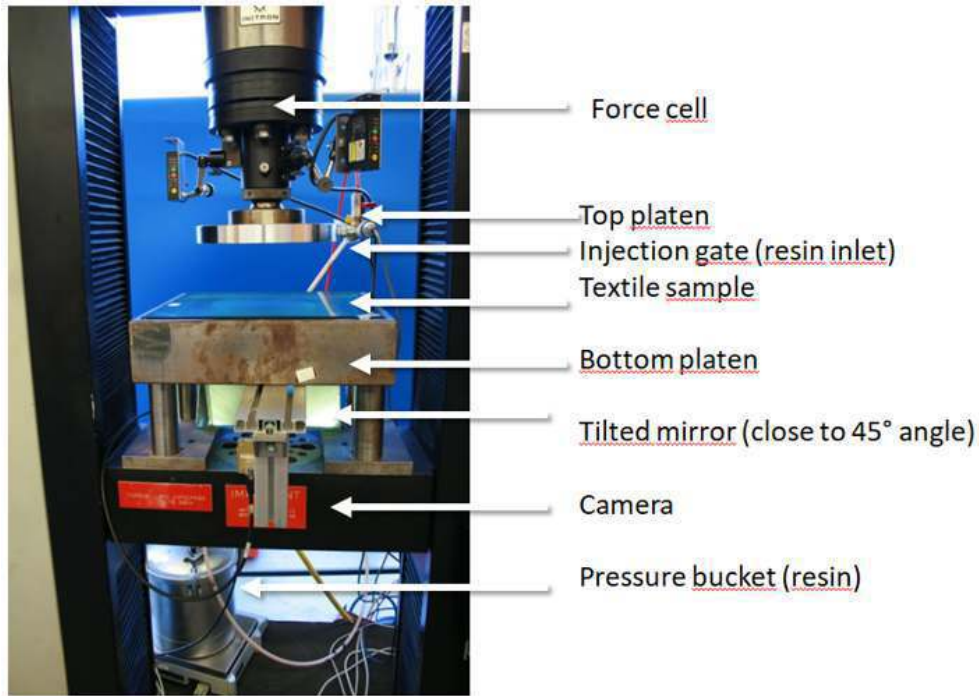


Figure 3: Apparatus used for the central injection experiments [52].

2.4. Monitoring and acquisition

The camera is used to take images of the flow at specified times to identify the location of the flow front. These raw images are saved and treated to produce black and white images which can then be used to extract the location of the interface that will be used for later analysis. An example of the raw images showing the flow front evolution is shown in figure 4. The calibration of the camera has been made to correct optical barreling distortion and relate the pixel size to the material size.

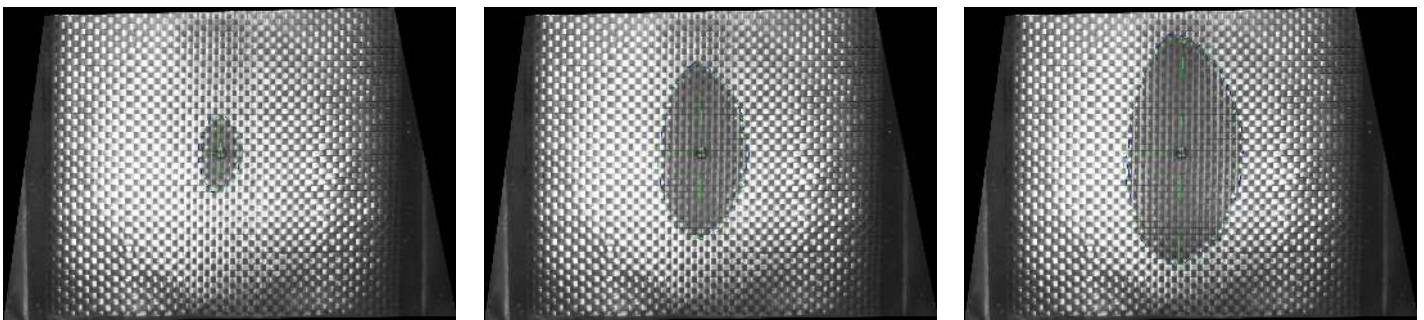


Figure 4: Raw flow front images at 3 different time instants of one of the central injection experiments. As time goes on, the liquid (grey central ellipse) flows into the porosity of the textile.

The corresponding treated segmented images are shown in figure 5.

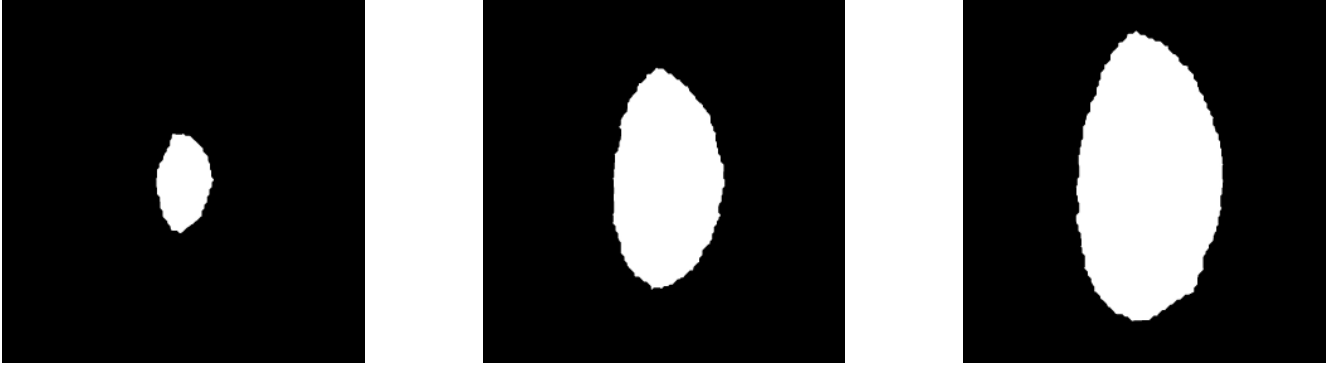


Figure 5: Treated flow front images at 3 different time instants of one of the central injection experiments, where the white part referred to resin impregnated textile and the black refers to dry textile.

A pressure sensor is located at the inlet that is used to measure the inlet liquid pressure profile as a function of time. This data will also be used in the algorithm for permeability predictions.

To summarize, the data from 34 central injection experiments includes

- flow front images with time (≈ 30 images per experiment),
- inlet pressure as a function of time,
- textile porosity and resin viscosity data,
- and a lightbox image of the fabric (2D plain weave) taken prior to injection.

2.5. Average permeability calculation

The average permeability of the textile samples (single plies) was measured following the procedure given by Swery et al. [52]; the mean and standard deviation of the measured values are shown in table 1.

Table 1: Mean and standard deviation of the permeability of the plain weave fibrous media used in the central injection experiments. These values are calculated by averaging the measured permeability values over the textile samples.

	k_{xx}	k_{yy}	k_{xy}
Mean ($10^{-10} m^2$)	0.69	3.28	0.078
Standard deviation ($10^{-10} m^2$)	0.12	0.57	0.054
Coefficient of variation	0.173	0.173	0.69

3. Governing equations

The problem at hand is an unsaturated flow in porous media problem in which the flow is governed by Darcy's law (1). During the mold filling process, the resin is injected into the mold displacing air outside. The outlet is designated with zero pressure, allowing air to escape freely. Additionally, the viscosity of air is much smaller than that of the resin, preventing any pressure buildup in the air region and thus fluid compressibility is negligible. As a result, the mass conservation equation simplifies to:

$$\nabla \cdot \mathbf{v} = 0. \tag{3}$$

Inlet and outlet pressure boundary conditions are assigned as follows:

$$p(\mathbf{x}_{inlet}, t) = p_{in}(t) \text{ on } \Gamma_{in} \quad (4)$$

$$p(\mathbf{x}_{outlet}, t) = p_{out}(t) \text{ on } \Gamma_{out} \quad (5)$$

To localize the interface (flow front), the volume of fluid (VOF) method [53, 54] is used. The method is based on defining a fraction function c , which is a scalar function that takes a value of 1 in the domain where resin exists, zero for the air, and values ranging from 0 to 1 near the interface between the phases. The interface is defined as the 0.5 level-set of the fraction function c . The more accurate the numerical method is, the smaller the interface region will be leading to a discontinuous fraction function in the ideal case. Using this definition, the viscosity μ in equation 1 can be rewritten as:

$$\mu = c\mu_r + (1 - c)\mu_a \quad (6)$$

where μ_r and μ_a are the viscosities of the resin and air, respectively. c evolves with time according to the following advection equation

$$\frac{\partial c}{\partial t} + \frac{1}{\phi} \mathbf{v} \cdot \nabla c = 0 \quad (7)$$

where $\frac{\partial c}{\partial t}$ is the time derivative of the fraction function c , ∇c its gradient in space and ϕ is the porosity of the porous medium.

Initial and boundary conditions need to be defined for the VOF advection equation. The initial condition is written as:

$$c(\mathbf{x}, t = 0) = c_0(\mathbf{x}). \quad (8)$$

The mold is assumed to be completely filled with air at $t = 0$; thus, $c_0 = 0$ for all \mathbf{x} .

Inlet flow also requires the assignment of boundary conditions for c :

$$c(\mathbf{x}_{inlet}, t) = 1 \text{ on } \Gamma_{in} \quad (9)$$

4. Methods

4.1. Neural network approximation of fields

The velocity \mathbf{v} , pressure p and resin volume fraction c fields for each experiments are approximated by feed forward neural networks having 5 hidden layers each with 20 neurons.

$$\mathbf{v}^{(j)} \approx \hat{\mathbf{v}}^{(j)}(x, y, t; \theta_v^{(j)}) \quad ; \quad p^{(j)} \approx \hat{p}^{(j)}(x, y, t; \theta_p^{(j)}) \quad ; \quad c^{(j)} \approx \hat{c}^{(j)}(x, y, t; \theta_c^{(j)}) \quad (10)$$

where j denotes the experiment index, while $\theta_v^{(j)}$, $\theta_p^{(j)}$ and $\theta_c^{(j)}$ are the trainable parameters of the networks. The hyperbolic tangent activation function is used for all the hidden layers of all the used networks. The output layer of $\hat{\mathbf{v}}^{(j)}$ has two units since the velocity field is a 2D vector field. Moreover, since the resin volume fraction c is naturally bounded between 0 and 1, a sigmoid activation is applied following the output layer of $\hat{c}^{(j)}$.

The permeability tensor is approximated using a CNN architecture:

$$\mathbf{K} \approx \hat{\mathbf{K}}(I; \theta_K) \quad (11)$$

Contrarily to velocity, pressure and resin fraction, the permeability model receives an $s \times s$ grayscale image $I \in \mathcal{R}^{s \times s}$ of the local textile configuration as an input and all the experiments share the same permeability model. The images I are obtained by cropping the original textile image $T \in \mathcal{R}^{S \times S}$ at centers specified by collocation points. In this work, $s = 50 \text{ px}$ and $S = 1150 \text{ px}$. The model outputs the three independent components of the 2D second order symmetric permeability tensor.

The CNN consists of convolutional, pooling, and fully-connected layers ending by the output, which is the permeability in this case. Batch normalization layers can also ensure that the inputs are well-normalized which improves the network performance. The trainable parameters of the network are denoted by θ_K . The following CNN architecture is adopted:

- Input layer of images having a size of 50×50 pixels,
- A convolutional layer with 8 filters of size 3×3 ,
- A Batch Normalization layer,
- An Average pooling layer of size 2×2 ,
- A convolutional layer with 16 filters of size 5×5 ,
- An Average pooling layer of size 2×2 ,
- A fully connected layer with 64 neurons and tanh activation function,
- An output layer with 3 neurons corresponding to k_{xx} , k_{yy} , and k_{xy} .

4.2. Choice of the collocation points

Collocation points are selected for residual evaluation of the PDEs at the centers of each pixel and at time frames given in the sequence. Therefore, the following notation is adopted:

$$x_l = (l - S/2) \cdot \Delta x \quad ; \quad y_m = (m - S/2) \cdot \Delta y \quad ; \quad t_n = n \cdot \Delta t \quad ; \quad (12)$$

where $\Delta x = \Delta y = 0.23 \text{ mm}$, $\Delta t = 2 \text{ s}$, $l, m = 0, 1, \dots, S - 1$ and $n = 0, 1, L - 1$ ($L = 30$). The global collocation index is also introduced as:

$$i = l + m \times S + n \times L. \quad (13)$$

Note that given a set (l, m, n) there is a unique corresponding global collocation index and vice versa, any i can be mapped back to a unique set (l, m, n) . Using i allows to introduce the following naming convention:

$$x_i, y_i, t_i = x_l, y_m, t_n, \quad (14)$$

leading to a simplification in the notation, allowing for the following expression:

$$\hat{\mathbf{v}}_i^j = \hat{\mathbf{v}}^{(j)}(x_i, y_i, t_i, \theta_v^{(j)}) = \hat{\mathbf{v}}^{(j)}(x_l, y_m, t_n, \theta_v^{(j)}). \quad (15)$$

Similarly, the notation for \hat{p}_i^j and \hat{c}_i^j can be simplified, indicating the evaluation of the pressure and resin fraction models at collocation point i for the j -th experiment.

Finally, denoted as

$$\hat{\mathbf{K}}_i^j = \hat{\mathbf{K}}(\mathbf{C}_s(T^j, x_l, y_m), \theta_K) \quad (16)$$

are the permeability values obtained by evaluating the CNN model at collocation point i for the j -th experiment, where $\mathbf{C}_s(T^j, x_l, y_m)$ is the $s \times s$ cropping operator acting on the j -th textile image and centered at (x_l, y_m) . It should be noted that a smaller random subset of the collocation points was used in practice.

4.3. Loss function

The loss function to be minimized includes both the physics loss from the governing equations and the data loss evaluated at a subset of N_{tc} collocation points across a number N_{te} of selected experiments for model training. A special treatment is due for the pressure boundary conditions as they must be enforced on a separate set of N_{bc} collocation points $(x_{\bar{i}}, y_{\bar{i}}, t_{\bar{i}})$ located on the domain boundaries. The loss can be formulated as follows:

$$\mathcal{L}(\theta_v^{(j)}, \theta_p^{(j)}, \theta_c^{(j)}, \theta_K) = \frac{1}{N_{te}} \sum_{j=0}^{N_{te}-1} \left(\lambda_c \mathcal{L}_c^j(\theta_c^{(j)}) + \lambda_p \mathcal{L}_p^j(\theta_p^{(j)}) + \lambda_1 \mathcal{L}_{f1}^j(\theta_v^{(j)}, \theta_p^{(j)}, \theta_K) + \lambda_2 \mathcal{L}_{f2}^j(\theta_v^{(j)}) + \lambda_3 \mathcal{L}_{f3}^j(\theta_c^{(j)}, \theta_v^{(j)}) \right) \quad (17)$$

where

$$\mathcal{L}_c^j(\theta_c^{(j)}) = \frac{1}{N_{tc}} \sum_{i=0}^{N_{tc}-1} \left(c_i^j - \hat{c}_i^j \right)^2 \quad (18)$$

is the training mean squared error (mse) of the j -th resin volume fraction model;

$$\mathcal{L}_p^j(\theta_p^{(j)}) = \frac{1}{N_{bc}} \sum_{i=0}^{N_{bc}-1} \left(p_i^j - \hat{p}^j(x_{\bar{i}}, y_{\bar{i}}, t_{\bar{i}}; \theta_p^{(j)}) \right)^2 \quad (19)$$

is the training mse of the j -th pressure model;

$$\mathcal{L}_{f1}^j(\theta_v^{(j)}, \theta_p^{(j)}, \theta_K) = \frac{1}{N_{tc}} \sum_{i=0}^{N_{tc}-1} \left(\hat{\mathbf{v}}_i^j + \frac{1}{\mu} \hat{\mathbf{K}}_i^j \cdot \nabla \hat{p}_i^j \right)^2 \quad (20)$$

is the training mean squared residual (msr) associated to the Darcy's law applied to the j -th model;

$$\mathcal{L}_{f2}^j(\theta_v^{(j)}) = \frac{1}{N_{tc}} \sum_{i=0}^{N_{tc}-1} \left(\nabla \cdot \hat{\mathbf{v}}_i^j \right)^2 \quad (21)$$

is the training msr associated with mass conservation of the j -th model and

$$\mathcal{L}_{f3}^j(\theta_c^{(j)}, \theta_v^{(j)}) = \frac{1}{N_{tc}} \sum_{i=0}^{N_{tc}-1} \left(\frac{\partial \hat{c}_i^j}{\partial t} + \hat{\mathbf{v}}_i^j \cdot \nabla \hat{c}_i^j \hat{\mathbf{v}}_i^j \right)^2 \quad (22)$$

is the training msr associated with the VOF transport equation applied to the j -th model. In practice, it was observed that any attempt to minimize the loss function in a monolithic way was leading to poor convergence regardless of the choice of the weighting coefficients λ_i . Therefore, a segregated sequential training strategy was devised, which is detailed in the next subsection.

4.4. Sequential training

The point of departure of the training strategy is to replace the permeability model evaluations $\hat{\mathbf{K}}_i^j$ with as many trainable parameters $\tilde{\mathbf{K}}_i^j$. As a consequence of this choice, the loss function introduced in the previous section can be minimized over each experiment separately. Segregating flow experiments and training the corresponding networks separately leads to a remarkably superior convergence. Namely, for the j -th experiment, the set of $\tilde{\mathbf{K}}_i^j$, $i = 0, 1, \dots, \tilde{N}_{tc}$ trainable permeabilities is denoted as \mathcal{K}^j . In doing so, only a fraction of the original collocation points is considered (i.e. the pixel centers) in order to avoid overfitting due to introducing too many new trainable parameters. The modified loss functions can be rewritten as :

$$\mathcal{L}^j(\theta_v^{(j)}, \theta_p^{(j)}, \theta_c^{(j)}, \mathcal{K}^j) = \lambda_c \mathcal{L}_c^j(\theta_c^{(j)}) + \lambda_p \mathcal{L}_p^j(\theta_p^{(j)}) + \lambda_1 \tilde{\mathcal{L}}_{f1}^j(\theta_v^{(j)}, \theta_p^{(j)}, \mathcal{K}^j) + \lambda_2 \mathcal{L}_{f2}^j(\theta_v^{(j)}) + \lambda_3 \mathcal{L}_{f3}^j(\theta_c^{(j)}, \theta_v^{(j)}) \quad (23)$$

with the modified Darcy loss

$$\tilde{\mathcal{L}}_{f1}^j(\theta_v^{(j)}, \theta_p^{(j)}, \mathcal{K}^j) = \frac{1}{\tilde{N}_{tc}} \sum_{i=0}^{\tilde{N}_{tc}-1} \left(\hat{\mathbf{v}}_i^j + \frac{1}{\mu} \tilde{\mathbf{K}}_i^j \cdot \nabla \hat{p}_i^j \right)^2. \quad (24)$$

Minimizing the loss function in equation (23) over the parameters $\theta_v^{(j)}$, $\theta_p^{(j)}$, $\theta_c^{(j)}$ and \mathcal{K}^j is equivalent to solving an inverse problem using PINN to determine the permeability values. These values can be gathered from all the experiments to create a data set consisting of image-label pairs $(I_i^j; \tilde{\mathbf{K}}_i^j)$ and use this to train the CNN model to predict permeabilities from local textile structures. A second and most important advantage offered by the sequential training strategy is that proper filtering and augmentation techniques can be applied to the data, leading to improved accuracy and generalization of the CNN model. Ultimately, the model is evaluated using an unseen flow experiment left out of the training set. For this new case, the permeability is predicted based from the evaluation of CNN model on the dry textile image, then PINN is used as a forward solver to compute the flow variables and finally the predicted filling pattern is compared to the experiments using the metrics defined in section 5. To summarize, the training strategy consists of the following steps, also shown in figure 6:

1. Training PINNs for the permeability identification inverse problem followed by data filtering and augmentation.
2. Training a CNN model to learn the mapping from the porous media images to the identified permeability.
3. Assessing model accuracy through comparison of predicted and experimental filling patterns for new test data.

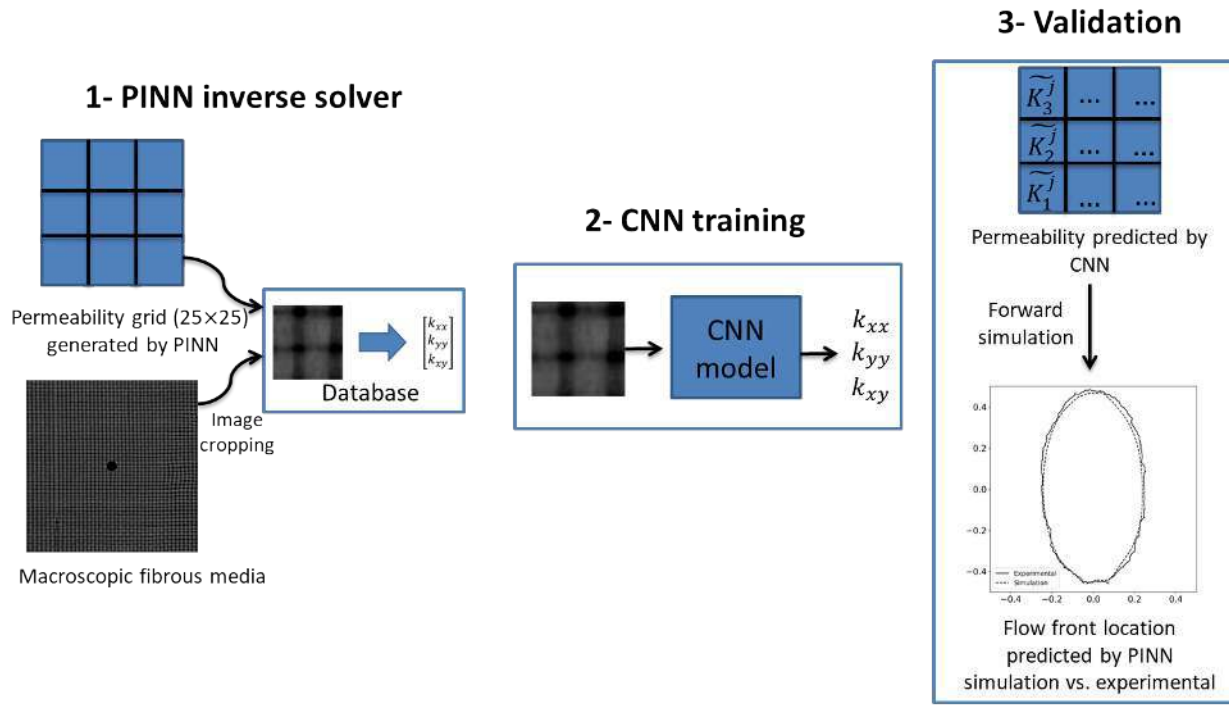


Figure 6: The full sequential training methodology to predict the permeability tensor field from textile images.

4.4.1. Identifying permeabilities using PINN

To solve the identification problem using PINN, different feedforward neural networks are used to approximate the pressure, fraction function, and the velocity, similar to the framework given by [31]. The computational domain is split into a grid of size 25×25 , in which each subdomain will have an unknown permeability tensor, hence in this case $\tilde{N}_{tc} = 625$. The subdomains' size is chosen to be small enough to capture the locality of the flow, however, a too-small subdomain size will create too many degrees of freedom and overfitting can easily take place. The chosen size is based on having at least one plain-weave periodic pattern (1 : 2 tows per warp and weft direction) in each crop, and when trying it in practice it provided good results. These unknown permeabilities are treated similarly to the network parameters: after initialization, values are updated using the minimization algorithm. The collocation points will have different permeabilities according to the subdomain they belong to.

Adam optimizer is used for 5000 iterations which is followed by 500 BFGS iterations. Figure 7 shows the full PINN framework to solve the inverse problem.

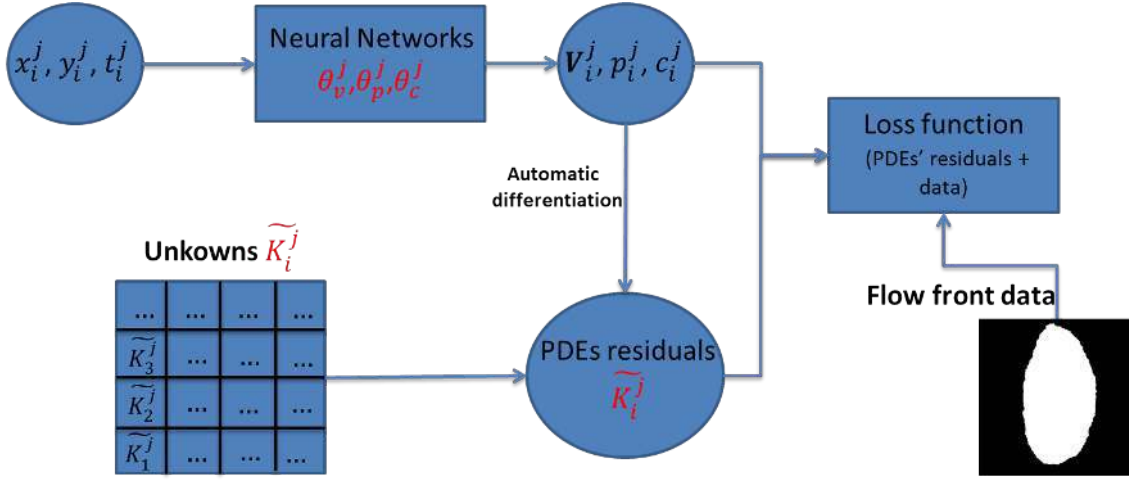


Figure 7: The framework to identify the permeability field by solving an inverse problem with PINN. The trainable parameters are identified in red.

An example of the identified permeability map is shown in figure 8 for one of the experiments.

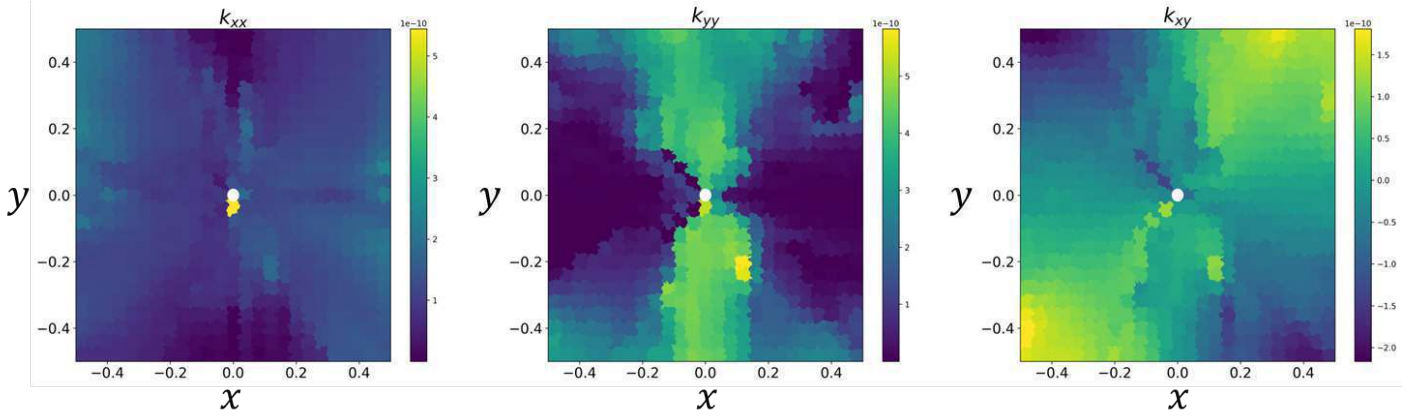


Figure 8: Example of the identified permeability field obtained by solving an inverse problem with PINN. The permeability component k_{xx} , k_{yy} , and k_{xy} are plotted from left to right, respectively. The x and y axes have been normalized; the real material size is $27 \times 27 \text{cm}^2$

It is important to note that only a portion of the permeability field is utilized in generating these flow-front predictions, and there are certain regions within the field that cannot be considered trustworthy. Hence, a process of data cleaning is conducted, which will be elaborated upon and discussed in the subsequent section.

4.4.1.1 Permeability data cleaning

To enhance the reliability of the permeability data, a data cleaning procedure is implemented to eliminate information in which there is less confidence. One such type of data is associated with the porous media locations where the resin did not reach during the experiment. Consequently, the inferred permeability data in these regions cannot be considered valid. After excluding these unreliable data points, the resulting trustworthy areas are displayed in figure 9.

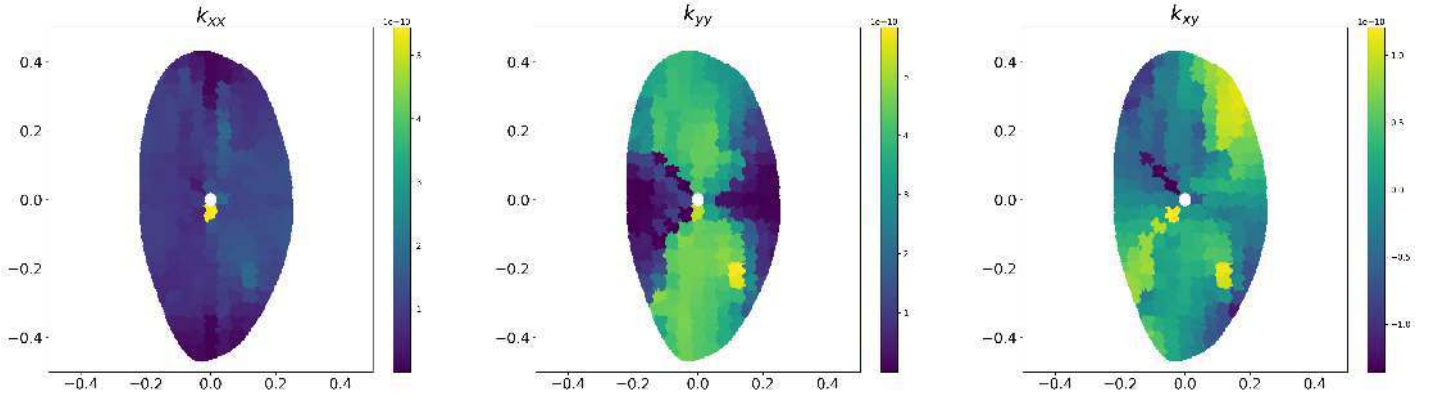


Figure 9: Example of the identified permeability field after trimming the regions where the resin did not reach. The permeability component k_{xx} , k_{yy} , and k_{xy} are plotted from left to right, respectively.

There is another category of data that is deemed untrustworthy, which pertains to the locations along the x and y axes. Specifically, in the case of k_{xx} , the data along the y -axis is considered unreliable since k_{xx} does not play a role in determining the flow in that direction. Similarly, for k_{yy} , the values along the x -axis are not trusted. The resulting version of the data that is considered trustworthy, after removing these unreliable values, is presented in figure 10.

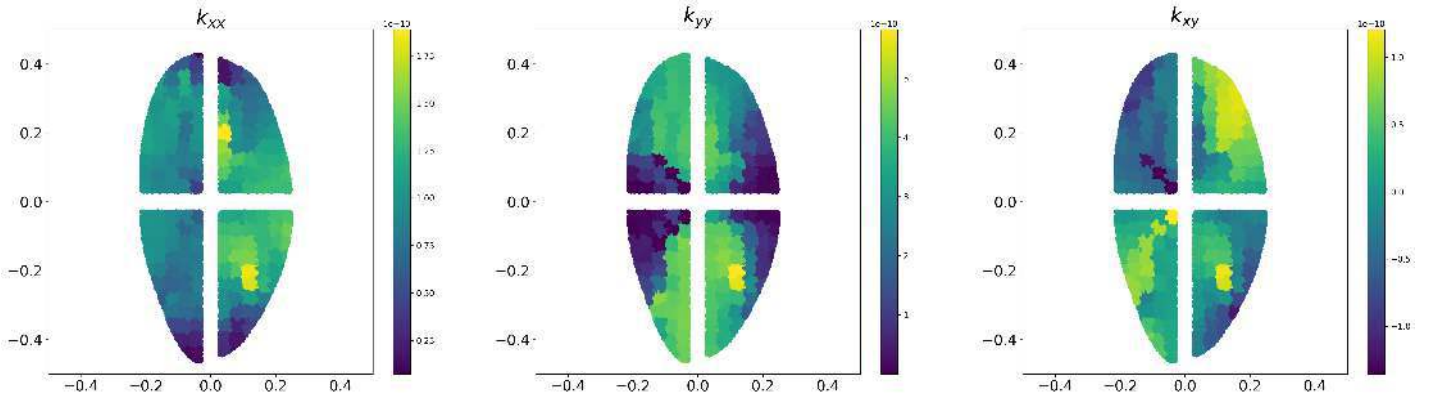


Figure 10: Example of the identified permeability field after all the trimming of the untrusted data. The permeability component k_{xx} , k_{yy} , and k_{xy} are plotted from left to right, respectively.

It should be noted that even though the data of k_{xx} along the x -axis and k_{yy} along the y -axis are trustworthy, in fact the most trustworthy in the data, they were removed so that each location have full permeability tensor information; so that one convolutional neural network can be used for the permeability tensor prediction.

4.4.1.2 Permeability data augmentation

The data that will be used in training the convolutional network is the lightbox images as in figure 2 and the cleaned permeability data as in figure 10. The lightbox images are cropped in 50×50 pixels images, where each crop corresponds to a permeability region. The data is, then, organized as a list of image crops and corresponding permeability tensors.

Data augmentation is used in order to increase the amount and variety of data used in the training. Rotation of 90° and 180° is performed on the cropped images and the permeability tensor is rotated accordingly. The rotated permeability is obtained through the following equation:

$$\mathbf{K}_{\text{rot}} = \mathbf{R}^T \mathbf{K} \mathbf{R}, \quad (25)$$

where \mathbf{R} is a rotation tensor that reads as:

$$\mathbf{R} = \begin{bmatrix} \cos(\theta) & -\sin(\theta) \\ \sin(\theta) & \cos(\theta) \end{bmatrix} \quad (26)$$

and θ is the angle of rotation.

The original dataset form along with the augmented data is shown in figure 11.

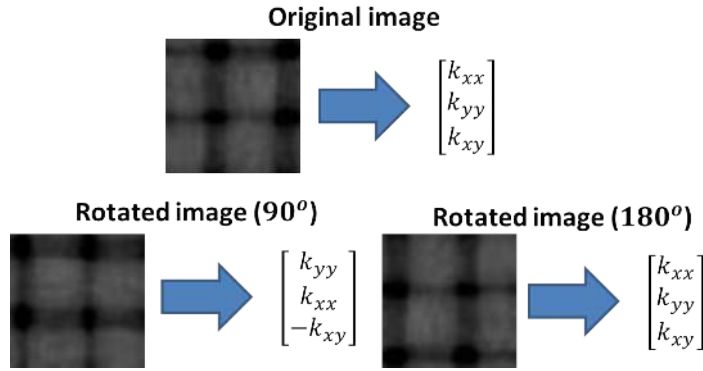


Figure 11: A sample of the data to be used for the convolutional neural network training which includes a lightbox cropped image and the corresponding permeability tensor labels. On top, one can find the cropped image and corresponding permeability tensor labels, and at the bottom, the augmented data through applying rotation of 90° and 180° along with rotated permeability tensor data.

4.4.2. Training the CNN permeability model

The CNN is trained from scratch on the cleaned and augmented dataset obtained from the previous stage. The dataset size obtained from 33 experiments (one experiment is left out for testing purposes) is about 18,000. This is split into training and validation sets with a ratio of 9 : 1. L_2 normalization is applied to all the trainable parameters in the network to avoid overfitting. Mean absolute error is used as the loss function to be minimized. Adam minimization algorithm is used for 1000 epochs with an initial learning rate of 0.001, with a batch size of 128. In the training process, convergence is determined upon observing a divergence between the training and validation errors for over 100 consecutive iterations. The model associated with the minimal validation error is subsequently retained for testing.

4.4.3. Model evaluation

To validate the developed model, leave one out cross-validation (LOOCV) method [55] is used to ensure that the model is not biased and the predictions are accurate regardless of the chosen test set. To this end, one of the 34 experiments is left out for testing and the training procedure is done using the remaining 33 experiments. After the model is trained, it is used to predict the permeability of the left-out test. The predicted permeability is used to perform forward simulation using PINN and the results are compared to the existing experimental flow front images. The results of the simulation using the CNN-predicted permeability field are also compared with the simulation using an average experimental measure of the permeability. This process is repeated for all 34 tests, where the CNN is retrained from scratch every time using a different test, and the training set is changed accordingly. The algorithm below clarifies the model evaluation process.

Algorithm 1: Deatiled procedure for the leave one out cross validation methodology.

Leave 1 experiment as a test set;

i=0;

while ($i < 34$) **do**

- train the CNN using the rest 33 experiments;
- Make permeability prediction of the left-out test;
- Perform simulation using the predictions and compare with experiments;
- change the left-out test and change the training set accordingly;
- i=i+1;

end

Two different error measures are used to assess the performance of the model. The first is the absolute difference between the experimental flow front image at the final time step and the simulation results which measures the percentage of the mispredicted pixels, referred to as e_p and defined as:

$$e_p = \frac{\int_{\Omega} 2|c - c_{exp}| d\mathbf{X}}{\int_{\Omega} c d\mathbf{X} + \int_{\Omega} c_{exp} d\mathbf{X}}, \quad (27)$$

where c is the fraction function solution using the permeability prediction method and c_{exp} is the fraction function from the experiment.

The second error uses the Hausdorff distance [56] which is a measure of the distance between two shapes (set of points), in this case the predicted flow front shape compared to the experimental flow front shape. The Hausdorff distance between two sets X and Y is defined as:

$$d_H(X, Y) = \max \left\{ \sup_{x \in X} (\inf_{y \in Y} d(x, y)), \sup_{y \in Y} (\inf_{x \in X} d(x, y)) \right\}, \quad (28)$$

where sup represents the supremum, inf the infimum, and where $d(x, y)$ quantifies the distance from a point $x \in X$ to a point $y \in Y$. Figure 12 can help to visually understand the two error definitions given two curves (flow front shapes), X and Y .

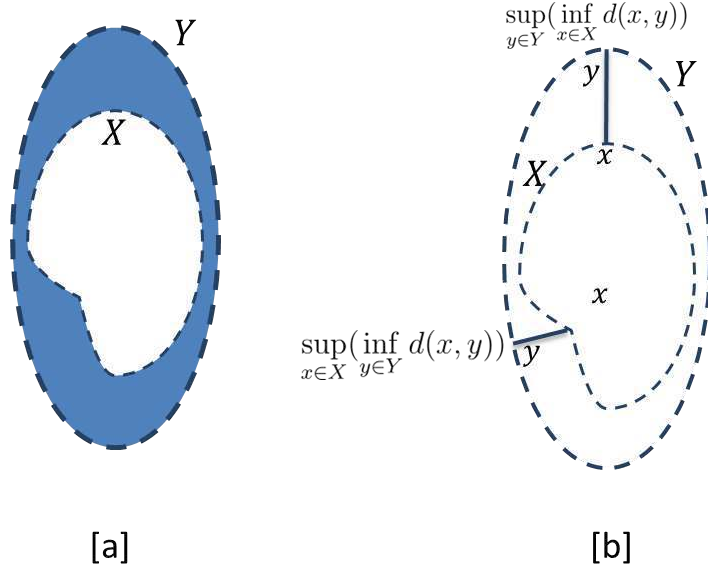


Figure 12: [a] A graphical representation of the error e_p , where the shaded area between the two flow front shapes, X and Y , represents the mispredicted pixels. [b] The Hausdorff distance between two curves, X and Y [57].

Following the definition of the Hausdorff distance, the second error measure, referred to as e_d , can be defined as:

$$e_d = \frac{H_d}{H_0} \quad (29)$$

where H_d is the Hausdorff distance between the model and experimental flow front, and H_0 is the Hausdorff distance from the experimental flow front shape to its center of mass which is used for normalization.

5. Results

The two error metrics distributions are plotted for all 34 tests in histograms (figures 13 and 14). The y -axis represents the number of occurrences and the x -axis represents the error in percentage.

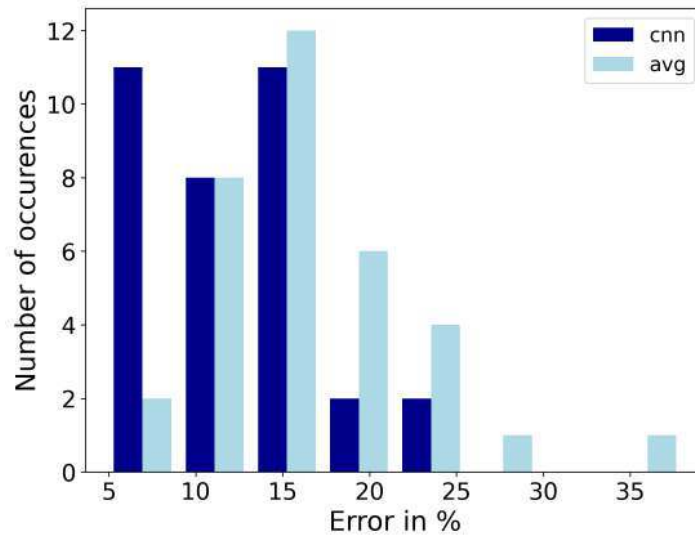


Figure 13: Histogram plot showing the number of occurrences in the y -axis and the mispredicted pixels error e_p measure in percentage in the x -axis for the simulation using CNN-predicted permeability and the simulation using the average permeability.

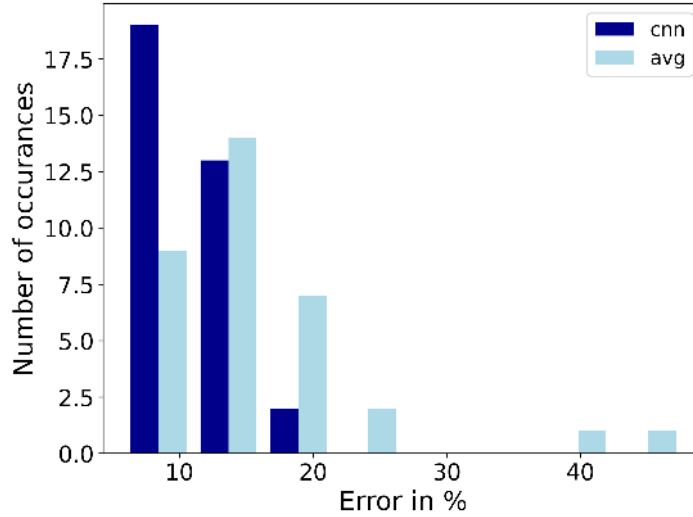


Figure 14: Histogram plot showing the number of occurrences in the y -axis and the shape error e_d measure in percentage in the x -axis for the simulation using CNN-predicted permeability and the simulation using the average permeability.

Regarding the first error metric e_p , the developed CNN model produced prediction errors in the 34 tests with a mean of 12% and a standard deviation of 5%. While the uniform permeability model produced errors with a mean of 16% and a standard deviation of 6%. Concerning the second error measure e_d , the CNN model produced errors in the 34 tests with a mean of 11% and a standard deviation of 3%. While the uniform permeability model produced errors with a mean of 15.6% and a standard deviation of 6%. It can be seen from the two error figures that CNN results have a high probability of producing low errors ($< 10\%$) and there is a low probability of having high error. For the results using an average value of the permeability, there is a low probability of getting very low errors and the error distribution follows a normal distribution trend with errors centered nearly 15% for the 2 error measures. It can be concluded that using the CNN predicted permeability field there is a higher probability that the predicted flow front matches the reality as compared to using a single average value.

In general, the central injection of plain-weave fabrics results in an anisotropic elliptical flow behavior according to experiments. In some of the test cases, the experimental injection front has a shape close to an ellipse, meaning that there are low local defects or variability. Both the CNN and the average permeability produced comparable results as in test case number 21 plotted in figure 15. In this test, the CNN produced an error of 6.6%, while the average permeability produced an error of 12.1% using the mispredicted pixels error. Using the shape error, the CNN produced an error of 5.8%, while the average permeability produced an error of 9.0%.

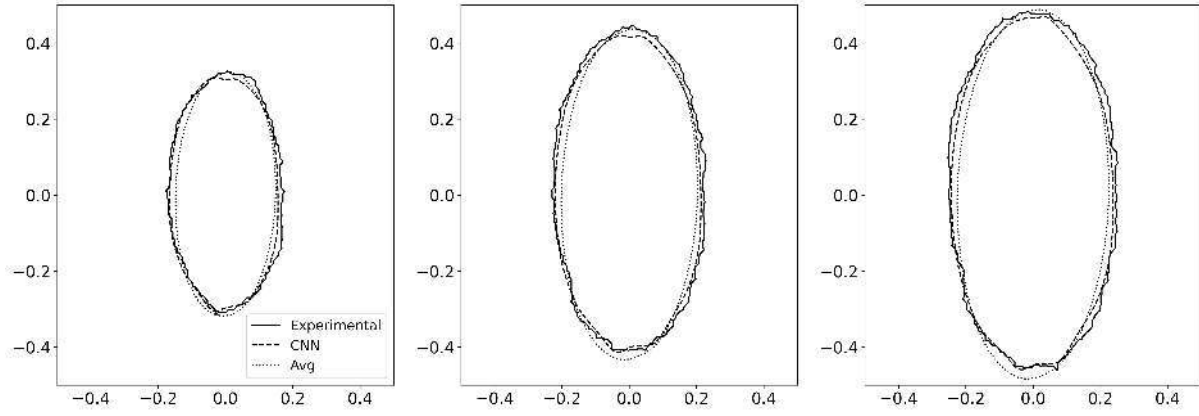


Figure 15: Flow front positions at three different time instants for the experimental, simulation using the CNN-predicted permeability, and simulation using average permeability for test number 21.

If there is high local variability, it is expected that the experimental flow will not follow the ideal elliptical shape. Two test cases are shown where the experimental flow fronts are not elliptical and exhibit less anisotropic behavior. It could be due to local features such as gaps or misorientation between tows in the samples. The two tests, numbers 24 and 26, are plotted in figures 16 and 17, simultaneously. The CNN managed to accurately capture these features from the images producing a good prediction for the permeability which was proven by the accurate flow simulation that matched the experimental flow front shape. As opposed to the results using an average permeability which, by essence, could not capture this effect.

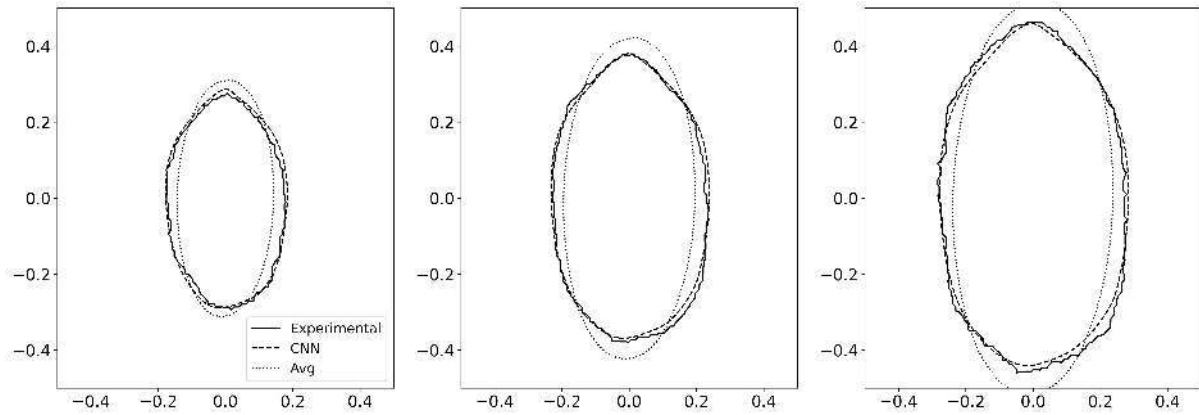


Figure 16: Flow front location at 3 different time instants of experiments number 24. The figures show the experimental flow front along with the simulated flow front using the CNN predicted permeability and the measured average permeability value.

For test number 24, the CNN produced an error of 5.3%, while the average permeability produced an error of 20.5% using the mispredicted pixels error. Using the shape error, the CNN produced an error of 7.4%, while the average permeability produced an error of 16.0%.

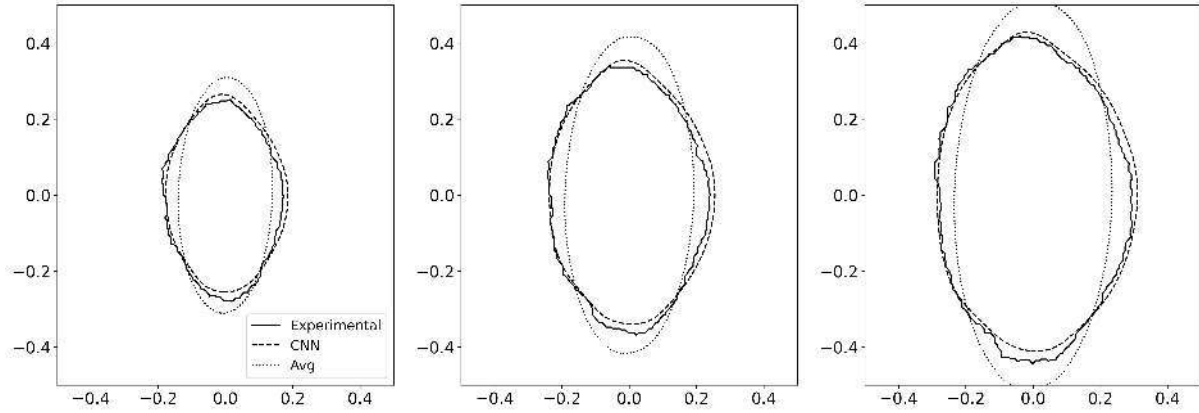


Figure 17: Flow front location at 3 different time instants of experiments number 26. The figures show the experimental flow front along with the simulated flow front using the CNN predicted permeability and the measured average permeability value.

For test number 26, the CNN produced an error of 6.9%, while the average permeability produced an error of 26.2% using the mispredicted pixels error. Using the shape error, the CNN produced an error of 9.2%, while the average permeability produced an error of 24.2%.

6. Conclusion and perspectives

6.1. Conclusion

A method to predict the permeability field from macroscale fibrous porous media images is introduced. This in turn can be used to perform accurate simulations for flow in porous media capturing flow effects due to local permeability variations. The results obtained in this study are promising and can easily be transferred to a different field with different types of porous media. Extension to 3D porous media is an expected evolution of the presented work, although data acquisition might be more difficult for this case.

Two main advantages of the present technique can be concluded. The first is the ability to make predictions of the permeability field capturing the local effects within one part and also capturing the variability from one part to another. The second is the possibility of using the same trained CNN to predict the permeability field of any 2D geometry since the training is performed on image crops of the big macroscale image. Even though this needs experimental testing but it is an obvious possible advantage to the method.

6.2. Perspectives

This work opens three main potential perspectives. The first perspective is the possibility of generalizing the technique to predict the permeability for any planar geometry. The second is applying the technique to a different thin fibrous textile other than the plain weave which was used in the data generation and model training. The third is the extension of the method to thick or curved textiles.

6.2.1. Training and Prediction for planar geometries

The primary advantage and strength of the presented technique lie in establishing a connection between the macroscopic geometry image and the localized small image crops. Through training the CNN on these image crops, the model gains the ability to predict the permeability field for any 2D planar geometry with any injection strategy.

The image crops, irrespective of the macroscopic geometry, exhibit consistent characteristics. This consistency enables the prediction of the permeability field for an arbitrary 2D planar geometry, making it independent of the specific geometric configuration. In essence, the presented method is local and therefore "geometry agnostic," meaning it can potentially handle diverse geometries without requiring specific adaptations or modifications.

Moreover, in this article, the training has been performed with central injection experiments. But any other injection strategy (peripheral, multi-gates...) could be used during the training phase.

6.2.2. Generalization for other thin textiles

In this study, the training of the CNN involved utilizing data obtained from experiments conducted on a plain weave textile. To enhance the data set and improve the model's ability to generalize, data augmentation techniques were employed. However, a crucial question remains regarding the model's performance when applied to different fibrous media structures such as, for instance, twill weaves, braided architectures, or even in-plane sheared materials. Verifying this generalization necessitates conducting experiments specifically designed to test for these materials.

By training the model on different fibrous textiles, the generalization of the model will be enhanced. In addition, it will be valuable in the future to expand the training set by incorporating data of textiles in unsheared and sheared configurations. This broader training approach would allow the model to learn and adapt to the features present in different fibrous textiles and deformation configurations.

Finally, for structural composite applications many plies of textiles are laid-up. Depending on the nature of the textiles, more or less nesting takes place. For these configurations, the model can be trained with the superposition of the local areal weights from the images of each single plies and injections of the corresponding multiple ply-stacks.

6.2.3. Extension to thick or curved textiles

The method presented in this work could be extended to thick textiles. The training procedure can be numerically extended to thick textiles and 3D flows. However, the bottlenecks will mostly rely on the experimental testing procedures in 3D domains in which data acquisition in the 3D volume is needed. Moreover, expensive 3D imaging techniques will be required (such as X-ray tomography) so as to have a proper textile geometrical description and dedicated sensing for flow front evolution.

For deployment on curved thin shell-like structures, the model does not require further training. We would need images from multiple points of view of the curved textile to identify the "flattened" textile crops [58, 59, 60]. Once this is addressed, the proposed framework in this paper could be developed to curved thin structures. Of course, for highly curved textiles, the latter could exhibit in-plane deformations such as shearing. For the scenario, further training in sheared configuration will have to be performed. One option is to train in planar and sheared configuration or to train in curved configuration. For training in curved configuration, we would have to ensure that the flow images can be mapped back to the curved geometry. There has been work in the literature considering the extension of PINN to curved thin structures for solid mechanics applications [61].

Acknowledgements

This study was funded under the PERFORM Thesis program of IRT Jules Verne.

References

- [1] Q. Govignon, S. Bickerton, P. Kelly, Liquid composite molding processes, in: *Advanced Fiber-Reinforced Polymer (FRP) Composites for Structural Applications*, Elsevier, 2023, pp. 101–136.
- [2] T. Mesogitis, A. A. Skordos, A. Long, Uncertainty in the manufacturing of fibrous thermosetting composites: A review, *Composites Part A: Applied Science and Manufacturing* 57 (2014) 67–75.
- [3] S. Konstantopoulos, C. Hueber, I. Antoniadis, J. Summerscales, R. Schledjewski, Liquid composite molding reproducibility in real-world production of fiber reinforced polymeric composites: A review of challenges and solutions, *Advanced Manufacturing: Polymer & Composites Science* 5 (3) (2019) 85–99.
- [4] R. Arbter, J. Beraud, C. Binetruy, L. Bizet, J. Bréard, S. Comas-Cardona, C. Demaria, A. Endruweit, P. Ermanni, F. Gommer, et al., Experimental determination of the permeability of textiles: A benchmark exercise, *Composites Part A: Applied Science and Manufacturing* 42 (9) (2011) 1157–1168.
- [5] N. Vernet, E. Ruiz, S. Advani, J. B. Alms, M. Aubert, M. Barburski, B. Barari, J. M. Beraud, D. C. Berg, N. Correia, et al., Experimental determination of the permeability of engineering textiles: Benchmark ii, *Composites Part A: Applied Science and Manufacturing* 61 (2014) 172–184.
- [6] D. May, A. Aktas, S. Advani, D. Berg, A. Endruweit, E. Fauster, S. Lomov, A. Long, P. Mitschang, S. Abaimov, et al., In-plane permeability characterization of engineering textiles based on radial flow experiments: A benchmark exercise, *Composites Part A: Applied Science and Manufacturing* 121 (2019) 100–114.
- [7] ISO 4410:2023, Test methods for the experimental characterization of in-plane permeability of fibrous reinforcements for liquid composite moulding, International Organization for Standardization, Geneva, Switzerland, 2023.
- [8] E. Syerko, T. Schmidt, D. May, C. Binetruy, S. Advani, S. Lomov, L. Silva, S. Abaimov, N. Aissa, I. Akhatov, et al., Benchmark exercise on image-based permeability determination of engineering textiles: Microscale predictions, *Composites Part A: Applied Science and Manufacturing* 167 (2023) 107397.
- [9] S. Comas-Cardona, B. Cosson, S. Bickerton, C. Binetruy, An optically-based inverse method to measure in-plane permeability fields of fibrous reinforcements, *Composites Part A: Applied Science and Manufacturing* 57 (2014) 41–48.
- [10] B. Cosson, Optical measurement of local permeability of flax fiber fabrics before liquid composite molding, *Journal of Composite Materials* 52 (24) (2018) 3289–3297.
- [11] P. C. Carman, Fluid flow through granular beds, *Chemical Engineering Research and Design* 75 (1997) S32–S48.
- [12] T. G. Gutowski, Z. Cai, S. Bauer, D. Boucher, J. Kingery, S. Wineman, Consolidation experiments for laminate composites, *Journal of Composite Materials* 21 (7) (1987) 650–669.
- [13] T. G. Gutowski, T. Morigaki, Z. Cai, The consolidation of laminate composites, *Journal of Composite Materials* 21 (2) (1987) 172–188.
- [14] B. R. Gebart, Permeability of unidirectional reinforcements for rtm, *Journal of composite materials* 26 (8) (1992) 1100–1133.

- [15] S. Sharma, D. A. Siginer, Permeability measurement methods in porous media of fiber reinforced composites, *Applied Mechanics Reviews* 63 (2) (2010).
- [16] K. K. Han, C. W. Lee, B. P. Rice, Measurements of the permeability of fiber preforms and applications, *Composites science and Technology* 60 (12-13) (2000) 2435–2441.
- [17] Y. Lee, J. Wu, Y. Hsu, C. Chung, A prediction method on in-plane permeability of mat/roving fibers laminates in vacuum assisted resin transfer molding, *Polymer composites* 27 (6) (2006) 665–670.
- [18] K. Adams, W. Russel, L. Rebenfeld, Radial penetration of a viscous liquid into a planar anisotropic porous medium, *International Journal of Multiphase Flow* 14 (2) (1988) 203–215.
- [19] J. Weitzenböck, R. Sheno, P. Wilson, Radial flow permeability measurement. part a: Theory, *Composites Part A: Applied Science and Manufacturing* 30 (6) (1999) 781–796.
- [20] M. Yun, H. Sas, P. Simacek, S. G. Advani, Characterization of 3d fabric permeability with skew terms, *Composites Part A: Applied Science and Manufacturing* 97 (2017) 51–59.
- [21] N. Takano, M. Zako, T. Okazaki, K. Terada, Microstructure-based evaluation of the influence of woven architecture on permeability by asymptotic homogenization theory, *Composites science and technology* 62 (10-11) (2002) 1347–1356.
- [22] L. Silva, G. Puaux, M. Vincent, P. Laure, A monolithic finite element approach to compute permeability at microscopic scales in lcm processes, *International Journal of Material Forming* 3 (2010) 619–622.
- [23] A. Nabovati, E. W. Llewellyn, A. C. Sousa, A general model for the permeability of fibrous porous media based on fluid flow simulations using the lattice boltzmann method, *Composites Part A: Applied Science and Manufacturing* 40 (6-7) (2009) 860–869.
- [24] H. Cho, N. Jeong, H. J. Sung, Permeability of microscale fibrous porous media using the lattice boltzmann method, *International Journal of heat and fluid flow* 44 (2013) 435–443.
- [25] R. Roscher, B. Bohn, M. F. Duarte, J. Garcke, Explainable machine learning for scientific insights and discoveries, *Ieee Access* 8 (2020) 42200–42216.
- [26] J. Wei, X. Chu, X.-Y. Sun, K. Xu, H.-X. Deng, J. Chen, Z. Wei, M. Lei, Machine learning in materials science, *InfoMat* 1 (3) (2019) 338–358.
- [27] M. Raissi, P. Perdikaris, G. E. Karniadakis, Physics-informed neural networks: A deep learning framework for solving forward and inverse problems involving nonlinear partial differential equations, *Journal of Computational Physics* 378 (2019) 686–707.
- [28] E. Haghighat, M. Raissi, A. Moure, H. Gomez, R. Juanes, A physics-informed deep learning framework for inversion and surrogate modeling in solid mechanics, *Computer Methods in Applied Mechanics and Engineering* 379 (2021) 113741.
- [29] M. Raissi, A. Yazdani, G. E. Karniadakis, Hidden fluid mechanics: Learning velocity and pressure fields from flow visualizations, *Science* 367 (6481) (2020) 1026–1030.

- [30] A. Kovacs, L. Exl, A. Kornell, J. Fischbacher, M. Hovorka, M. Gusenbauer, L. Breth, H. Oezelt, D. Praetorius, D. Suess, et al., Magnetostatics and micromagnetics with physics informed neural networks, *Journal of Magnetism and Magnetic Materials* 548 (2022) 168951.
- [31] J. M. Hanna, J. V. Aguado, S. Comas-Cardona, R. Askri, D. Borzacchiello, Residual-based adaptivity for two-phase flow simulation in porous media using physics-informed neural networks, *Computer Methods in Applied Mechanics and Engineering* 396 (2022) 115100.
- [32] J. M. Hanna, J. V. Aguado, S. Comas-Cardona, R. Askri, D. Borzacchiello, Sensitivity analysis using physics-informed neural networks, arXiv preprint arXiv:2301.02428 (2023).
- [33] Z. Mao, A. D. Jagtap, G. E. Karniadakis, Physics-informed neural networks for high-speed flows, *Computer Methods in Applied Mechanics and Engineering* 360 (2020) 112789.
- [34] I. Depina, S. Jain, S. Mar Valsson, H. Gotovac, Application of physics-informed neural networks to inverse problems in unsaturated groundwater flow, *Georisk: Assessment and Management of Risk for Engineered Systems and Geohazards* 16 (1) (2022) 21–36.
- [35] K. Ishitsuka, W. Lin, Physics-informed neural network for inverse modeling of natural-state geothermal systems, *Applied Energy* 337 (2023) 120855.
- [36] Y. Chen, L. Lu, G. E. Karniadakis, L. Dal Negro, Physics-informed neural networks for inverse problems in nano-optics and metamaterials, *Optics express* 28 (8) (2020) 11618–11633.
- [37] V. Oommen, B. Srinivasan, Solving inverse heat transfer problems without surrogate models: a fast, data-sparse, physics informed neural network approach, *Journal of Computing and Information Science in Engineering* 22 (4) (2022) 041012.
- [38] A. Serebrennikova, R. Teubler, L. Hoffellner, E. Leitner, U. Hirn, K. Zojer, Transport of organic volatiles through paper: physics-informed neural networks for solving inverse and forward problems, *Transport in Porous Media* 145 (3) (2022) 589–612.
- [39] A. D. Jagtap, Z. Mao, N. Adams, G. E. Karniadakis, Physics-informed neural networks for inverse problems in supersonic flows, *Journal of Computational Physics* 466 (2022) 111402.
- [40] N. Srisutthiyakorn*, Deep-learning methods for predicting permeability from 2d/3d binary-segmented images, in: SEG technical program expanded abstracts 2016, Society of Exploration Geophysicists, 2016, pp. 3042–3046.
- [41] K. M. Graczyk, M. Matyka, Predicting porosity, permeability, and tortuosity of porous media from images by deep learning, *Scientific reports* 10 (1) (2020) 21488.
- [42] C. Chueh, A. Bertei, J. Pharoah, C. Nicolella, Effective conductivity in random porous media with convex and non-convex porosity, *International Journal of Heat and Mass Transfer* 71 (2014) 183–188.
- [43] Z. Li, S. Galindo-Torres, G. Yan, A. Scheuermann, L. Li, A lattice boltzmann investigation of steady-state fluid distribution, capillary pressure and relative permeability of a porous medium: Effects of fluid and geometrical properties, *Advances in water resources* 116 (2018) 153–166.

- [44] H. Wu, W.-Z. Fang, Q. Kang, W.-Q. Tao, R. Qiao, Predicting effective diffusivity of porous media from images by deep learning, *Scientific reports* 9 (1) (2019) 20387.
- [45] J. Wu, X. Yin, H. Xiao, Seeing permeability from images: fast prediction with convolutional neural networks, *Science bulletin* 63 (18) (2018) 1215–1222.
- [46] T. Cawte, A. Bazylak, A 3d convolutional neural network accurately predicts the permeability of gas diffusion layer materials directly from image data, *Current Opinion in Electrochemistry* (2022) 101101.
- [47] P. Tang, D. Zhang, H. Li, Predicting permeability from 3d rock images based on cnn with physical information, *Journal of Hydrology* 606 (2022) 127473.
- [48] M. Elmorsy, W. El-Dakhkhni, B. Zhao, Generalizable permeability prediction of digital porous media via a novel multi-scale 3d convolutional neural network, *Water Resources Research* 58 (3) (2022) e2021WR031454.
- [49] S. Gärttner, F. O. Alpak, A. Meier, N. Ray, F. Frank, Estimating permeability of 3d micro-ct images by physics-informed cnns based on dns, *Computational Geosciences* 27 (2) (2023) 245–262.
- [50] B. Caglar, G. Broggi, M. A. Ali, L. Orgéas, V. Michaud, Deep learning accelerated prediction of the permeability of fibrous microstructures, *Composites Part A: Applied Science and Manufacturing* 158 (2022) 106973.
- [51] J. Gan, S. Bickerton, M. Battley, Quantifying variability within glass fibre reinforcements using an automated optical method, *Composites Part A: Applied Science and Manufacturing* 43 (8) (2012) 1169–1176.
- [52] E. E. Swery, T. Allen, S. Comas-Cardona, Q. Govignon, C. Hickey, J. Timms, L. Tournier, A. Walbran, P. Kelly, S. Bickerton, Efficient experimental characterisation of the permeability of fibrous textiles, *Journal of composite materials* 50 (28) (2016) 4023–4038.
- [53] C. W. Hirt, B. D. Nichols, Volume of fluid (vof) method for the dynamics of free boundaries, *Journal of computational physics* 39 (1) (1981) 201–225.
- [54] C. Swaminathan, V. Voller, A time-implicit filling algorithm, *Applied Mathematical Modelling* 18 (2) (1994) 101–108.
- [55] T.-T. Wong, Performance evaluation of classification algorithms by k-fold and leave-one-out cross validation, *Pattern recognition* 48 (9) (2015) 2839–2846.
- [56] W. Rucklidge, *Efficient visual recognition using the Hausdorff distance*, Springer, 1996.
- [57] J. Pellerin, *Accounting for the geometrical complexity of structural models in voronoi-based meshing methods*, Ph.D. thesis, Université de Lorraine (2014).
- [58] Y. Wang, N. Deng, B. Xin, W. Wang, W. Xing, S. Lu, A novel three-dimensional surface reconstruction method for the complex fabrics based on the mvs, *Optics & Laser Technology* 131 (2020) 106415.
- [59] Y. Kita, N. Kita, Virtual flattening of a clothing surface by integrating geodesic distances from different three-dimensional views., in: *VISIGRAPP (5: VISAPP)*, 2019, pp. 541–547.
- [60] R. Grossmann, N. Kiryati, R. Kimmel, Computational surface flattening: a voxel-based approach, *IEEE Transactions on Pattern Analysis and Machine Intelligence* 24 (4) (2002) 433–441.

- [61] J.-H. Bastek, D. M. Kochmann, Physics-informed neural networks for shell structures, *European Journal of Mechanics-A/Solids* 97 (2023) 104849.